Journal of Alloys and Compounds 1026 (2025) 180534

Contents lists available at ScienceDirect

Journal of Alloys and Compounds

journal homepage: www.elsevier.com/locate/jalcom

# Photothermal synergistic overall water splitting via non-noble nickel cocatalyst on $SrTiO_3$

Xuan Zhu, Yuan Gao, Jianan Hong, Entao Zhang, Yu Xie, Jia Mao, Chenyu Xu, Yanwei Zhang *

*State Key Laboratory of Clean Energy Utilization, Zhejiang University, Hangzhou 310027, China*

## ARTICLE INFO

*Keywords:*
Photothermal catalysis
Noble-metal-free
Synergistic mechanism
Overall water splitting
Perovskite

## ABSTRACT

The synergistic coupling of optical and thermal effects for the comprehensive utilization of solar energy has garnered increasing attention in recent research. In this work, the synergistic coupling of solar photo and thermal effects was realized using a non-noble metal Ni cocatalyst loaded with Mg and Al codoped $SrTiO_3$. In the photothermal synergistic decomposition of pure water, the efficiencies of $H_2$ and $O_2$ reached 1.011 $mmol\cdot g^{-1}\cdot h^{-1}$ and 0.497 $mmol\cdot g^{-1}\cdot h^{-1}$, respectively. The hydrogen yield was almost 2.7 times higher than that of pure photocatalysis. It was found that the introduction of NiOOH significantly enhanced the separation and migration of photogenerated carriers, along with the significant thermal effect. A series of variable temperature characterizations confirm that the thermal effect in sunlight can enhance light absorption and reduce the carrier transport impedance of material, which significantly improves carrier utilization and further promotes hydrogen generation. This study provides an effective idea for the design of solar non-noble metal catalysts for hydrogen production by utilizing the photothermal synergy strategy.

## 1. Introduction

The world is currently grappling with severe environmental challenges, including climate change, air pollution, and resource depletion, all of which are intrinsically linked to the extensive reliance on fossil fuels [1–3]. As a result, the development of clean, renewable energy sources has become a global imperative. Among these, solar energy stands out as a clean and abundant resource, making it a key area of research in global energy science [4–8]. Photothermal catalytic water splitting presents an efficient approach to solar energy utilization, enabling the direct conversion of widely available water resources into hydrogen and oxygen without producing pollutants [9–12]. As a clean energy carrier, hydrogen has high energy density and broad application potential, positioning it as a key energy source to drive the energy transition and achieve sustainable development in the future [13,14]. However, conventional semiconductor photocatalysts are constrained by their wide band gaps, which restrict them to using only the ultraviolet portion (290–400 nm) of the solar spectrum, which accounts for merely 5 % of the total solar energy. In contrast, nearly 50 % of the solar energy resides in the infrared region (>760 nm), which cannot excite semiconductor materials to generate photogenerated charge carriers for water splitting. Instead, this infrared energy is absorbed by the material lattice and manifests itself as a temperature increase [15]. This temperature change affects the radiative properties of the semiconductor, which in turn affects the catalytic performance. Therefore, the study of the synergistic mechanisms of optical and thermal effects under solar irradiation is essential for enhancing the efficiency of water splitting and advancing the practical application of solar energy.

Strontium titanate ($SrTiO_3$), a wide bandgap semiconductor with a perovskite structure, has attracted increasing research interest due to its suitable band alignment and tunable material properties [16–18]. Recent studies have demonstrated that doping with low-valence cations can effectively enhance the water splitting activity of $SrTiO_3$. Domen et al. employed $Al^{3+}$ doping in combination with a high-temperature melting strategy to successfully reduce $Ti^{3+}$ defects. This high-temperature melting process also facilitated the recrystallization of $SrTiO_3$, exposing crystal facets with specific activity, which significantly improved the photocatalytic water splitting performance [19]. Chang et al. applied a co-doping strategy with $La^{3+}$ and $Al^{3+}$, observing that the introduction of $La^{3+}$ facilitated the reincorporation of surface-extracted $Sr^{2+}$ ions back into the perovskite lattice, further reducing $Ti^{3+}$ defects and enhancing water splitting efficiency [20]. Our previous work has

---

* Corresponding author.
*E-mail address:* zhangyw@zju.edu.cn (Y. Zhang).

https://doi.org/10.1016/j.jallcom.2025.180534
Received 22 February 2025; Received in revised form 17 April 2025; Accepted 19 April 2025

also confirmed that the introduction of Mg and Al into $SrTiO_3$ can increase the oxygen vacancy concentration and thus increase the water splitting activity [21]. However, all of the above catalysts incorporated the cocatalyst Rh, and the scarcity and high cost of noble metals limit their large-scale applications. In contrast, nickel, a commonly available transition metal, offers advantages such as low cost and superior catalytic performance [22]. Furthermore, Ni and its oxides exhibit significant thermal effects, which can effectively elevate the reaction temperature [23]. As such, non-noble metal Ni is a suitable choice of cocatalyst for the realization of photothermal synergistic utilization.

In this study, a catalyst that integrates both optical and thermal effects has been developed, featuring a non-noble NiOOH cocatalyst supported on Mg and Al codoped $SrTiO_3$ for photothermal overall water splitting. The incorporation of NiOOH cocatalyst can effectively enhance the absorption of the full spectrum of the material and improve the photoeffects of the material, and at the same time reduce the radiative composite of the material, which facilitates the rapid migration of the charge carriers. Meanwhile, NiOOH also effectively enhanced the photothermal response of the catalyst, with the surface temperature increasing by 40°C compared to the sample without the cocatalyst. Under photothermal synergistic conditions, the $H_2$ yield was enhanced by a factor of 2.7 relative to the pure photocatalytic reaction. To further investigate the influence of thermal effects on the catalyst performance, a series of temperature-dependent characterizations were conducted. It was found that the full-spectrum absorption of the catalyst was significantly enhanced with the increase in temperature, and the radiative recombination of carriers decreased, their mobility enhanced, the photocurrent increased, and the electrical impedance became smaller. Collectively, these changes contributed to the enhanced performance of photothermal synergistic water splitting. This study elucidates the synergistic mechanisms of optical and thermal effects in the NiOOH loaded MgAl codoped $SrTiO_3$ catalyst, providing valuable insights into the enhancement of photothermal catalytic water splitting using non-precious metals.

## 2. Experimental section

### 2.1. Chemicals and materials

Nanostrontium titanate ($SrTiO_3$, 99.5 % metal basis, < 100 nm) was purchased from Meryer Biochemical Technology Co., Ltd.). (Shanghai). Strontium chloride ($SrCl_2$, 99.0 % purity) was purchased from Leyan (Shanghai Haohong Scientific Co., Ltd.). Nanosized magnesium oxide (MgO, 99.9 % metal basis) was purchased from Macklin (Biochemical Co., Ltd). (Shanghai). Nickel nitrate hexahydrate ($Ni(NO_3)_2 \bullet 6\ H_2O$) was purchased from Aladdin (Biochemical Technology Co., Ltd.). (Shanghai).

### 2.2. Synthesis of catalysts

The properties and preparation methods of Mg Al codoped $SrTiO_3$ have been studied in detail in our previous work [21]. Specifically, $SrTiO_3$, MgO, and $SrCl_2$ were mixed by grinding in an agate crucible for a certain time at molar ratios of 1:0.01:10. The mixture was then transferred to an alumina crucible and calcined in a muffle furnace at 1423 K for 10 hours in air. The sample was then rinsed with water to remove excess $SrCl_2$ and dried to obtain the desired substrate, and the obtained MgAl codoped $SrTiO_3$ sample (Al was provided by the $Al_2O_3$ crucible) will be abbreviated as MgAlSTO in the following text. The cocatalysts were loaded using the in situ photodeposition method. A 50 mg sample was taken and dispersed in a volume of water for ultrasonic pretreatment, followed by continuous magnetic stirring in a beaker. Next, a defined mass fraction of $Ni(NO_3)_2 \bullet 6\ H_2O$ was added and irradiated under a xenon lamp. Finally, the suspension was dried by centrifugation to obtain the sample.

### 2.3. Characterizations

X-ray diffraction (XRD) patterns were acquired using a Rigaku SmartLab SE (Japan), equipped with a copper Kα radiation source operating at 40 kV and 40 mA. Scanning electron microscopy (SEM) was performed with a ZEISS GeminiSEM 360. High-resolution transmission electron microscopy (HR-TEM) coupled with energy-dispersive X-ray spectroscopy (EDX) was employed to investigate the sample's microstructure and elemental distribution, using a Thermo Scientific Talos-F200X G2 system. X-ray photoelectron spectroscopy (XPS) measurements were conducted with a Thermo Scientific K-Alpha instrument, utilizing an aluminum Kα radiation source (hv = 1486.6 eV). The metal content in the catalysts was quantified by inductively coupled plasma optical emission spectrometry (ICP-OES) using a Thermo Fisher iCAP PRO(OES) spectrometer. UV–visible diffuse reflectance spectroscopy (UV–vis DRS) was performed using Shimadzu UV-2600 and Shimadzu UV-3600 iPlus spectrophotometers. The recombination dynamics and carrier lifetime in the catalysts were analyzed through photoluminescence (PL) emission spectroscopy (JY HORIBA FluoroLog-3), with excitation provided by a 365 nm lamp.

### 2.4. Electrochemical measurements

To prepare the working electrode, 5 mg of the catalyst was dispersed in 1 mL of anhydrous ethanol with a few drops of Nafion solution, followed by ultrasonic treatment. The resulting suspension was uniformly deposited onto indium-tin oxide (ITO) conductive glass and allowed to dry. Electrochemical characterizations were performed using an IVIUMSTAT electrochemical workstation. A three-electrode configuration was employed, consisting of a platinum plate as the counter electrode, an Ag/AgCl electrode with saturated KCl as the reference electrode, and the catalyst-coated ITO as the working electrode. A 0.5 M $Na_2SO_4$ solution served as the electrolyte, and a 365 nm LED (Figure S1b) was used as the illumination source.

### 2.5. Photothermal catalytic water splitting measurements

The water splitting reaction was conducted in a closed gas circulation system, with the gaseous products analyzed using gas chromatography (GC) equipped with a thermal conductivity detector (Agilent 8720 A), and argon as the carrier gas. For the preparation of the catalytic membrane, 10 mg of the catalyst was dispersed in water via sonication, and the resulting mixture was deposited onto a quartz fiber filter membrane to form a catalytic layer with a 3 cm diameter. The membrane was subsequently placed in a quartz reactor with a specific volume of water to ensure its positioning at the gas–liquid interface (Figure S2a).

To investigate the influence of temperature on catalytic activity, an alternative reaction setup was employed, as illustrated in Figure S2b. In this configuration, a cotton layer served as a water transport medium, with the catalytic membrane positioned atop the cotton to facilitate photothermal catalytic water splitting. Perforated polyethylene foam was used as a support structure for the cotton within the reaction vessel. The reaction was initiated by obliquely incident light from a 365 nm LED, while a xenon lamp equipped with a UV–VIS cutoff filter (>800 nm) was employed to evaluate the temperature's effect on the reaction.

## 3. Results and discussion

### 3.1. Structure characterization

XRD was conducted to determine the phase composition and crystal structure of the synthesized catalysts. As illustrated in Fig. 1a, The diffraction patterns exhibited distinct peaks characteristic of $SrTiO_3$ within the 5°–90° scanning range. The primary diffraction peaks, located at 22.7°, 32.3°, 39.9°, 46.4°, 52.3°, 57.7°, 67.8°, 72.5°, 77.1°,

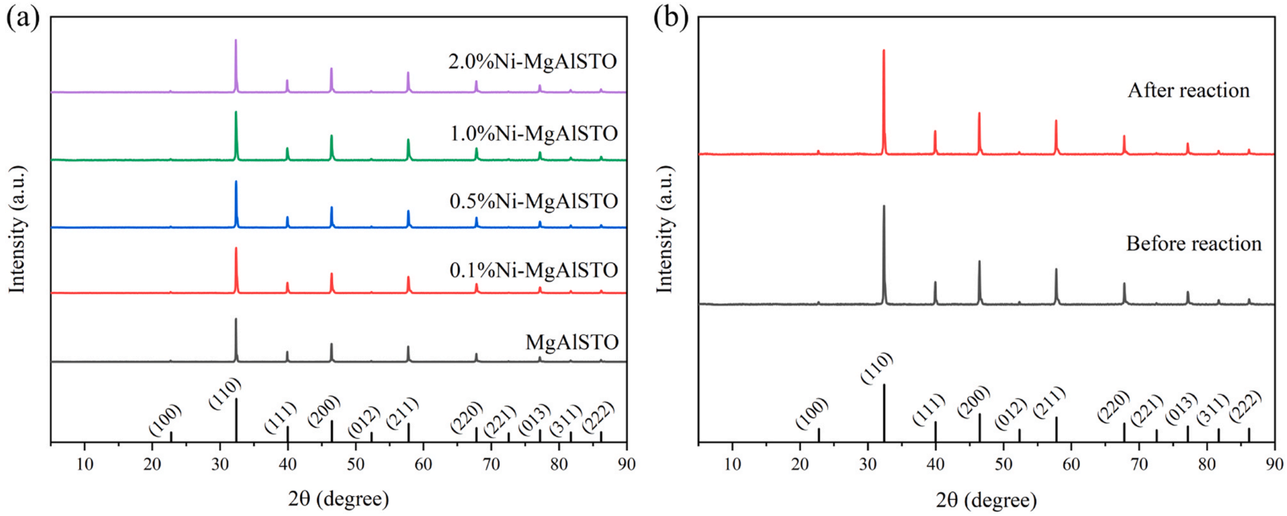

**Fig. 1.** (a) XRD patterns of the as-prepared catalysts; (b) XRD patterns of 0.5 %Ni-MgAlSTO before and after reaction.

81.7°, and 86.2°, correspond to the (100), (110), (111), (200), (012), (211), (220), (221), (013), (311), and (222) crystal planes, respectively, as indexed by the standard JCPDS card (No. 74–1296). The above results were consistent with our previous work, confirming the successful synthesis of MgAlSTO [21]. No discernible Ni-related diffraction peaks were observed in the Ni-based loaded catalysts, likely due to the low Ni content and its effective dispersion. Further analysis of the positions of the main diffraction peak positions in the Ni-loaded catalysts revealed that the peak corresponding to the (110) plane did not shift, and its shape remained unchanged. This indicates that the Ni element did not incorporate into the MgAlSTO lattice in the form of doping but instead was loaded on the surface of MgAlSTO. The stability of the crystal structure during the reaction process was evaluated by analyzing the 0.5 %Ni-MgAlSTO samples before and after the reaction. As shown in Fig. 1b, the diffraction peaks of the samples did not exhibit any significant shift or morphological change, indicating that the catalyst maintained its structural integrity throughout the photothermal synergistic reaction.

As shown in Figure S3, the SEM images reveal that the MgAlSTO sample, after high-temperature melt treatment, exhibits a characteristic cubic structure with particle sizes ranging from several hundred nanometers. The surface appears smooth, with no observable attachment of extraneous particles. According to previous studies, the green arrows correspond to the reduced crystal planes of $SrTiO_3$, while the white arrows point to the oxidized crystal planes [24,25]. The photogenerated electrons and holes produced in $SrTiO_3$ migrate to the respective crystal planes, and this spatial separation of reduction and oxidation reactions promotes efficient carrier migration. As the amount of Ni precursor increases, flakes emerge on the surface of the Ni-loaded MgAlSTO and subsequently accumulate. This phenomenon indicates that Ni elements were gradually loaded on the surface of $SrTiO_3$, forming a layered structure. In the 0.5 %Ni-MgAlSTO sample, a substantial quantity of flaky substances can be observed on the surface. As illustrated in Figure S3, these substances preferentially accumulate on the oxidized crystal planes of MgAlSTO. This finding was consistent with previous studies that have demonstrated the preferential deposition of $Co^{2+}$ on oxidized crystal surfaces during photodeposition [26]. Similarly, $Ni^{2+}$ has been observed to exhibit a comparable behavior, confirming the successful loading of elemental Ni as an oxidation cocatalyst on the surface of the MgAlSTO [27,28].

The lattice spacing of the material was subjected to meticulous examination through the use of TEM to confirm the microstructure of the nickel-modified MgAlSTO material. A representative MgAlSTO particle was selected for analysis, and its HRTEM image was presented in Fig. 2. The distinct lattice stripes with a lattice spacing of 0.276 nm were attributed to the (110) crystal plane of the $SrTiO_3$, which aligns with the findings of the XRD analysis [29]. Additionally, a layer of material was visible on the surface of MgAlSTO with a lattice spacing of 0.208 nm, which aligns with the (210) crystal plane of NiOOH [30]. Further, the 0.5 %Ni-MgAlSTO sample underwent EDS analysis, and the corresponding scanning results were shown in Fig. 2d-i. The elements Sr, Ti, Mg, Al, and O were uniformly distributed in the material, confirming the successful synthesis of perovskite-type MgAlSTO. However, the distribution of Ni was not uniform, as depicted in Fig. 2 h, with Ni primarily concentrated on a specific surface of the catalyst. This observation indicates that Ni was successfully loaded on the surface of MgAlSTO in the form of NiOOH.

The ICP-OES technique was employed to accurately quantify the elemental Ni content in the catalysts, and the results are summarized in Table S1. The mass fractions of Ni in the samples, designated as 0.1 %Ni-MgAlSTO, 0.5 %Ni-MgAlSTO, 1.0 %Ni-MgAlSTO, and 2.0 %Ni-MgAlSTO, were determined to be 0.08 %, 0.29 %, 0.46 %, and 0.94 %, respectively. Despite some degree of elemental loss during sample preparation, a clear positive correlation was observed between the Ni mass fraction and the Ni precursor loading, consistent with the SEM observations, which showed the progressive formation of flakes on the MgAlSTO surface as Ni precursor content increased. This further corroborates the successful loading of Ni onto the catalyst surface.

The XPS full spectrum signals of all the samples are illustrated in Figure S5. Characteristic peaks corresponding to the main elements, including O 1 s, Ti 2p, Sr 3d, and the C 1 s signal peaks that were added to correct the plots, can be identified. These signals confirm the successful synthesis of the MgAlSTO catalyst samples. For the Ni-loaded samples, the Ni 2p signals were significantly enhanced with increasing Ni content, providing further evidence for the effective incorporation of Ni into the catalysts. The high-resolution Ni 2p spectra of all samples are presented in Figure S6. The Ni 2p spectrum of 0.1 % Ni-MgAlSTO exhibited four distinct peaks: the Ni 2p3/2 peak (856.0 eV) and its corresponding satellite peaks, the Ni 2p1/2 peak (873.7 eV) and its satellite peaks. These peak positions indicate that Ni primarily exists as $Ni^{3+}$ ions in the catalysts [31]. Further analysis of the Ni 2p spectra of 0.5 % Ni-MgAlSTO, 1.0 %Ni-MgAlSTO and 2.0 %Ni-MgAlSTO samples revealed that the positions of the Ni 2p peaks in these samples did not shift appreciably, suggesting that the Ni valence state remained predominantly as $Ni^{3+}$ even as the Ni loading increased.

Figure S7 shows the O 1 s spectra of the MgAlSTO samples, revealing two distinct oxygen signals. The peak around 531.29 eV corresponds to adsorbed oxygen on the material’s surface, while the peak at

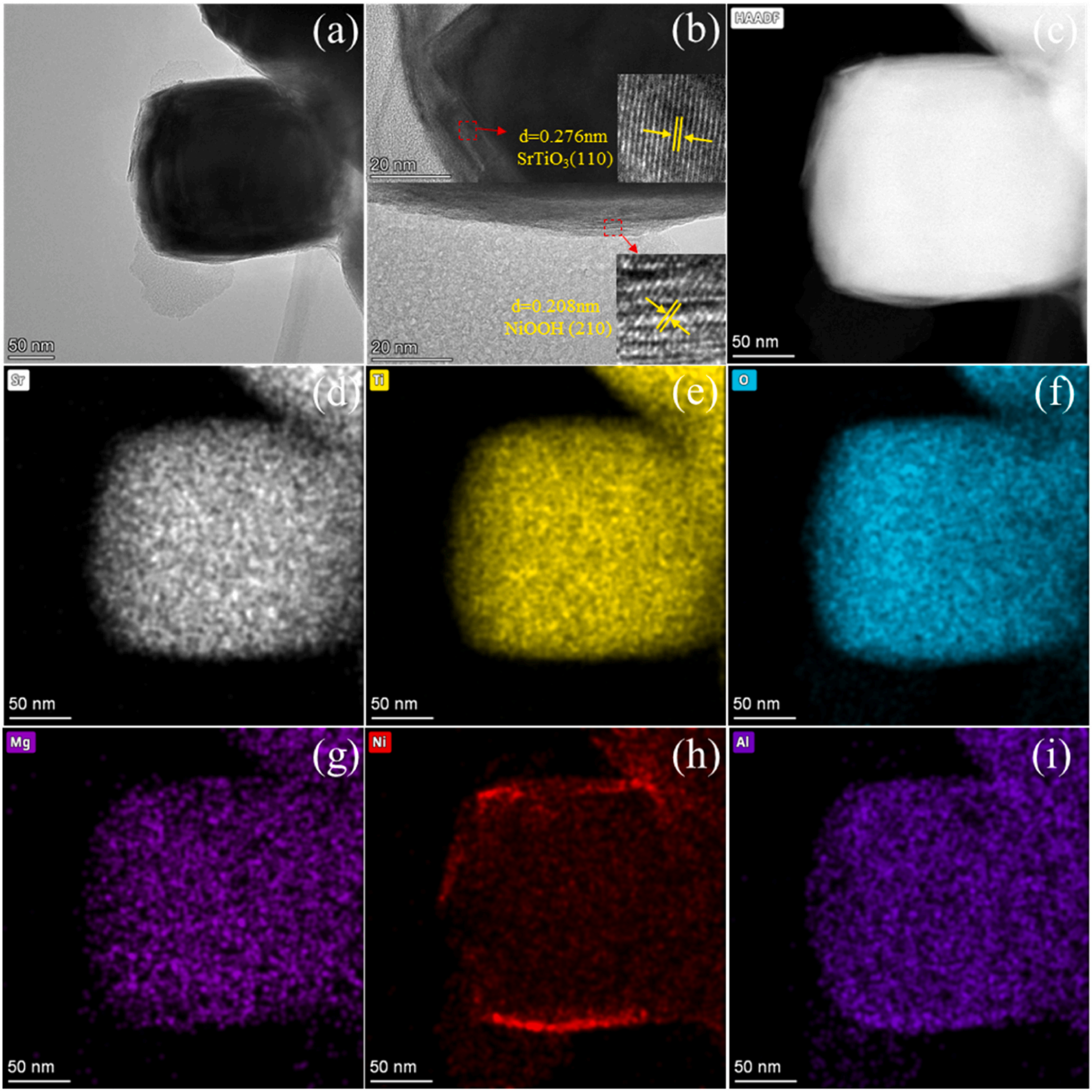

**Fig. 2.** (a-c) HRTEM image of a 0.5 %Ni-MgAlSTO particle; (d-i) EDS elemental mappings (strontium (Sr), titanium (Ti), oxygen (O), magnesium (Mg), nickel (Ni), aluminum (Al)).

approximately 529.10 eV was attributed to lattice oxygen within the material [20]. Upon Ni loading, the peak at approximately 531.6 eV was significantly enhanced for each sample, indicating an increase in surface OH groups [32]. This enhancement suggests that the NiOOH loading on the MgAlSTO surface contributed to a notable increase in OH species [28,33]. The XPS spectrum of Sr 3d for the MgAlSTO sample, shown in Figure S8, displays two peaks corresponding to Sr $3d_{3/2}$ and Sr $3d_{5/2}$, which reflect the spin-orbit splitting energy levels of Sr. Similarly, the Ti 2p spectrum shows two peaks corresponding to Ti $2p_{1/2}$ and Ti $2p_{3/2}$, representing the spin-orbit splitting of Ti. Following Ni loading, a shift in the Sr 3d and Ti 2p peaks was observed, indicating a strong interaction between the MgAlSTO substrate and the NiOOH cocatalyst [34]. To evaluate the stability of the catalyst before and after the reaction, XPS was performed on the 0.5 %Ni-MgAlSTO sample post-reaction, as shown in Figure S9. The positions and shapes of the primary peaks in the Ni 2p spectra remained unchanged, confirming that the Ni species remained stable throughout the photothermal reaction.

### 3.2. Experimental performance of photothermal catalysis

Under full-spectrum xenon lamp irradiation, the photothermal catalytic water splitting yields of $H_2$ and $O_2$ for all MgAlSTO samples were accurately measured. As shown in Fig. 3a, the MgAlSTO substrate exhibits negligible photocatalytic water splitting activity, with the yields of $H_2$ and $O_2$ being only 11.9 umol·g$^{-1}$·h$^{-1}$ and 6.1 umol·g$^{-1}$·h$^{-1}$, respectively. This was attributed to the lack of suitable active sites on the

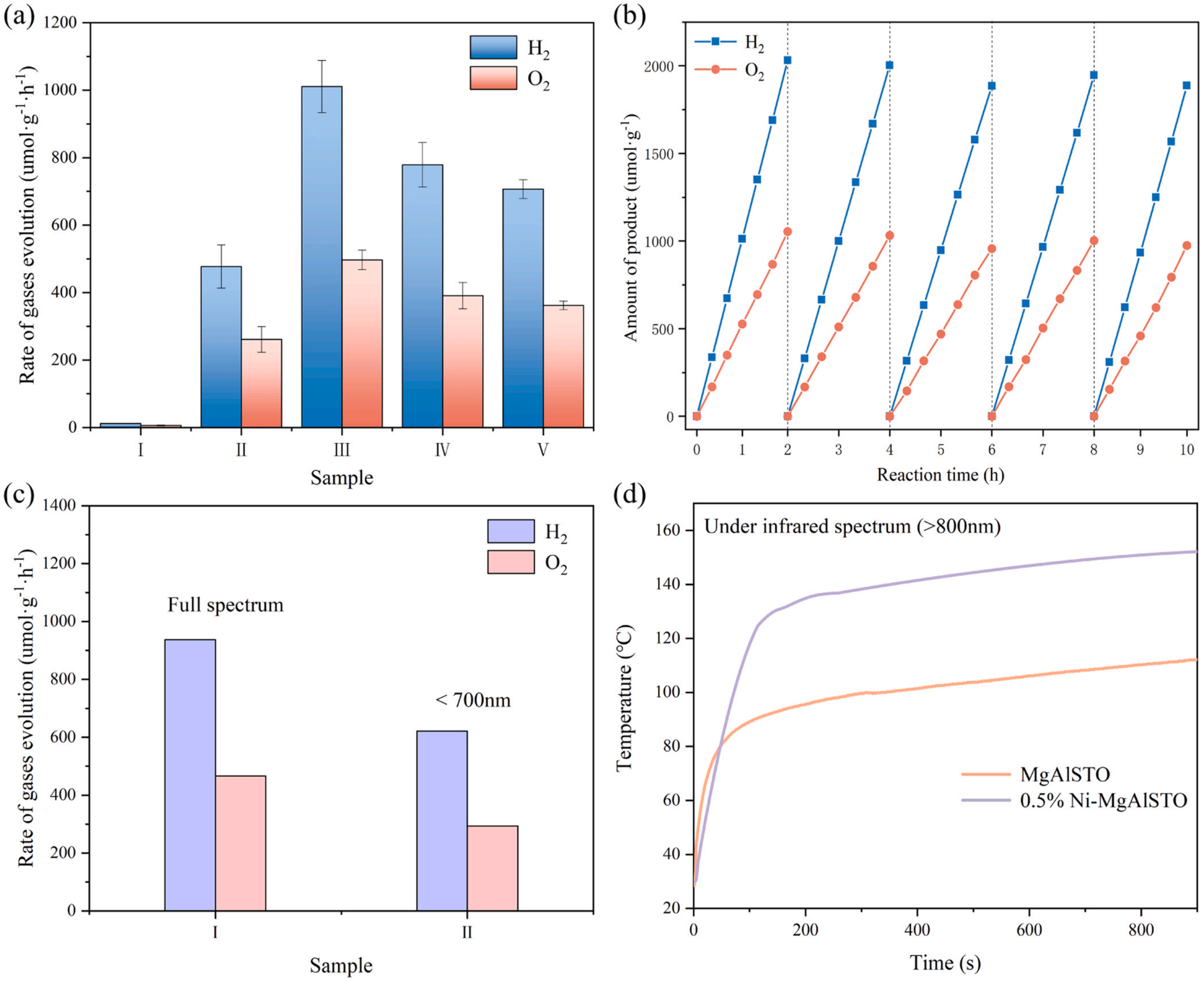

**Fig. 3.** (a) Corresponding $H_2$ and $O_2$ production rates [(I) MgAlSTO, (II) 0.1 %Ni-MgAlSTO, (III) 0.5 %Ni-MgAlSTO, (IV) 1.0 %Ni-MgAlSTO, (V) 2.0 %Ni-MgAlSTO]. (b) Stability tests of 0.5 %Ni-MgAlSTO.(c) Corresponding $H_2$ and $O_2$ production rates of 0.5 %Ni-MgAlSTO under different light sources (Sample I:Full spectrum; and II: < 700 nm).(d) Temperature variation curve with time under infrared spectrum irradiation (>800 nm).

surface of MgAlSTO, in which photogenerated electrons and holes generated by its absorption of sunlight are very easy to rapidly recombine and cannot reach the surface to effectively drive the water splitting reaction, thus limiting the generation of $H_2$ and $O_2$. When Ni was loaded on the surface of MgAlSTO in the form of NiOOH, water splitting activity significantly improved. NiOOH acts as an oxidation cocatalyst, facilitating the extraction of holes from the semiconductor, which promotes the separation of photogenerated charge carriers and participates in the water splitting process [35]. As shown in Fig. 3a, the yields of hydrogen and oxygen were 477.2 umol·g$^{-1}$·h$^{-1}$ and 261.2 umol·g$^{-1}$·h$^{-1}$ (0.1 % Ni-MgAlSTO), 1011.6 umol·g$^{-1}$·h$^{-1}$ and 497. 1 umol·g$^{-1}$·h$^{-1}$ (0.5 % Ni-MgAlSTO), 779.1 umol·g$^{-1}$·h$^{-1}$ and 391.7 umol·g$^{-1}$·h$^{-1}$ (1.0 % Ni-MgAlSTO), 707.21 umol·g$^{-1}$·h$^{-1}$ and 362.8 umol·g$^{-1}$·h$^{-1}$ (2.0 % Ni-MgAlSTO), respectively. Notably, $H_2$ and $O_2$ yields for all samples were produced in a stoichiometric ratio close to 2:1, confirming the photothermal catalytic overall water splitting capability of NiOOH-loaded MgAlSTO. Among these, the 0.5 %Ni-MgAlSTO sample exhibited the highest water splitting ability, with the hydrogen production activity 85 times greater than that of the MgAlSTO sample. However, as the NiOOH loading increased beyond 0.5 %, the water splitting activity decreased, likely due to the excessive NiOOH coverage on the MgAlSTO surface, which hindered the catalyst's interaction with water molecules. SEM analysis revealed that some particles in the 2.0 % Ni-MgAlSTO sample were almost completely encapsulated by the NiOOH layer, reducing the effective surface area for water interaction and consequently diminishing catalytic activity.

The stability of the catalyst was further evaluated, and as shown in Fig. 3b, the photocatalytic activity of the 0.5 %Ni-MgAlSTO sample remained nearly unchanged after 10 hours of continuous operation, indicating excellent stability for overall water splitting. In the photothermal water splitting process, light not only allows the catalyst to produce photogenerated electrons and holes but also produces thermal effects, which can significantly influence catalytic performance [36]. Fig. 3c presents the results of a control experiment using 0.5 %Ni-MgAlSTO as a representative catalyst. When the light source was filtered to exclude wavelengths above 700 nm, the hydrogen and oxygen yields decreased by approximately 34 % and 37 %, respectively, compared to full-spectrum irradiation. This phenomenon may be because the thermal effect of the infrared light part of the solar spectrum is more significant, which can effectively increase the temperature of the reaction system. If only the light source with a wavelength below 700 nm is used, the reaction temperature cannot be effectively increased, thereby inhibiting the activity of the water decomposition reaction. Considering the important role of the photothermal conversion characteristics of the catalyst in the photothermal catalytic reaction, the infrared light region with the most obvious thermal effect was selected as the simulated light source, and the changes in the surface temperature of the sample were monitored in real time by thermocouples. The experimental results are shown in Fig. 3d. At the moment the light source was turned on, the temperature of both samples increased rapidly and then stabilized. The sample with NiOOH showed a 40°C increase in surface temperature compared to the sample without the cocatalyst. This demonstrates that NiOOH not only enhances the photocatalytic activity of MgAlSTO but also contributes to a significant thermal effect that further elevates the temperature, enhancing the photothermal catalytic process.

To systematically evaluate the effect of temperature changes induced by the solar thermal effect on the reaction activity, an experiment was designed to investigate the photothermal catalytic water splitting performance of 0.5 %Ni-MgAlSTO under various temperature conditions. The reaction mode was shown in Figure S2b. A 365 nm wavelength LED lamp was used as the light source to drive the water decomposition reaction. At the same time, an 800 nm cutoff filter was used to filter the xenon lamp to ensure that only infrared light could pass through, thereby achieving temperature control of the catalytic reaction system. As illustrated in Fig. 4, when only the xenon lamp was activated, trace amounts of $H_2$ and $O_2$ were produced, indicating that infrared light alone could not effectively drive the water splitting reaction. When the 365 nm LED was turned on, the $H_2$ production rate increased rapidly, which was attributed to the strong absorption of UV light by this photocatalyst to drive the water decomposition reaction. When both the 365 nm LED and xenon lamp were turned on simultaneously, the sample was heated to the desired temperature by the thermal effect of the infrared light. The yields of $H_2$ at 313.15 K, 333.15 K, 353.15 K, 373.15 K, and 393.15 K were 114.7 $\mathrm{umol\cdot g^{-1}\cdot h^{-1}}$, 149.8 $\mathrm{umol\cdot g^{-1}\cdot h^{-1}}$, 199.4 $\mathrm{umol\cdot g^{-1}\cdot h^{-1}}$, 279.7 $\mathrm{umol\cdot g^{-1}\cdot h^{-1}}$, 315.4 $\mathrm{umol\cdot g^{-1}\cdot h^{-1}}$, respectively. The enhancement in $H_2$ yield due to the thermal effect was 26 % (333.15 K), 67 % (353.15 K), 137 % (373.15 K), and 167 % (393.15 K). Under the synergistic effect of light effect and thermal effect, the $H_2$ production rate increased from 114.7 umol/g/h under pure photocatalytic conditions to 315.4 umol/g/h, an increase of 2.7 times. The change in oxygen yield was shown in the Fig. 4b. The oxygen yields were 57.4 $\mathrm{umol\cdot g^{-1}\cdot h^{-1}}$, 76.9 $\mathrm{umol\cdot g^{-1}\cdot h^{-1}}$, 92.5 $\mathrm{umol\cdot g^{-1}\cdot h^{-1}}$, 136.6 $\mathrm{umol\cdot g^{-1}\cdot h^{-1}}$, and 158.8 $\mathrm{umol\cdot g^{-1}\cdot h^{-1}}$ at 313.15 K, 333.15 K, 353.15 K, 373.15 K, and 393.15 K, respectively. The increase in oxygen yield followed a trend similar to that of hydrogen production, maintaining a near stoichiometric ratio of 2:1 for $H_2$ and $O_2$. These results demonstrate that the thermal effect of infrared light significantly enhances photothermal catalytic water splitting, thereby increasing both hydrogen and oxygen yields. Therefore, the synergistic utilization of light effect and thermal effect can improve the conversion and utilization of solar energy.

### 3.3. *Characterization of the optical properties*

To comprehensively investigate the optical properties of different materials and their influence on the performance of photothermal synergistic hydrolysis reaction, the absorption spectra of all samples were analyzed by UV–visible spectrophotometer. As shown in Fig. 5a, the MgAlSTO samples exhibit strong light absorption in the UV region, indicating that the material can effectively absorb light and excite carriers under UV irradiation. However, when NiOOH was loaded on the surface of MgAlSTO, the material's light absorption in the UV region was significantly enhanced, suggesting that the presence of NiOOH facilitates the generation of more photogenerated carriers, thereby improving the water decomposition reaction and increasing the $H_2$ yield. Furthermore, with the increase of NiOOH loading, the spectral absorption of the material in the visible and infrared wavelength bands was gradually enhanced, which can significantly improve the photothermal conversion ability of the material. In the photothermal synergistic reaction, the light energy absorbed by the material not only excites electrons to generate photogenerated carriers but also converts into thermal energy, which in turn increases the catalytic surface temperature and promotes the water decomposition reaction [37]. As further corroborated by the temperature measurements in Fig. 3d. The addition of NiOOH resulted in a significant increase in the surface temperature of the material. The band gap of the material was obtained by calculating the absorption curves using the Kubelka-Munk equation [38]. As the NiOOH loading increased, the band gap gradually decreased, and the absorption edge was gradually red-shifted. This indicates that the NiOOH loading can enhance the light absorption ability of the material, leading to the generation of more photogenerated carriers for the water splitting reaction.

Photoluminescence spectroscopy was employed to measure the photogenerated carrier recombination of the catalytic materials. Fig. 6a shows the steady-state PL emission spectra obtained using laser excitation at 365 nm. The PL radiation intensity of the NiOOH loaded sample was significantly lower than that of the substrate material, indicating that the presence of NiOOH reduces the photogenerated carrier recombination and effectively promotes the separation of the

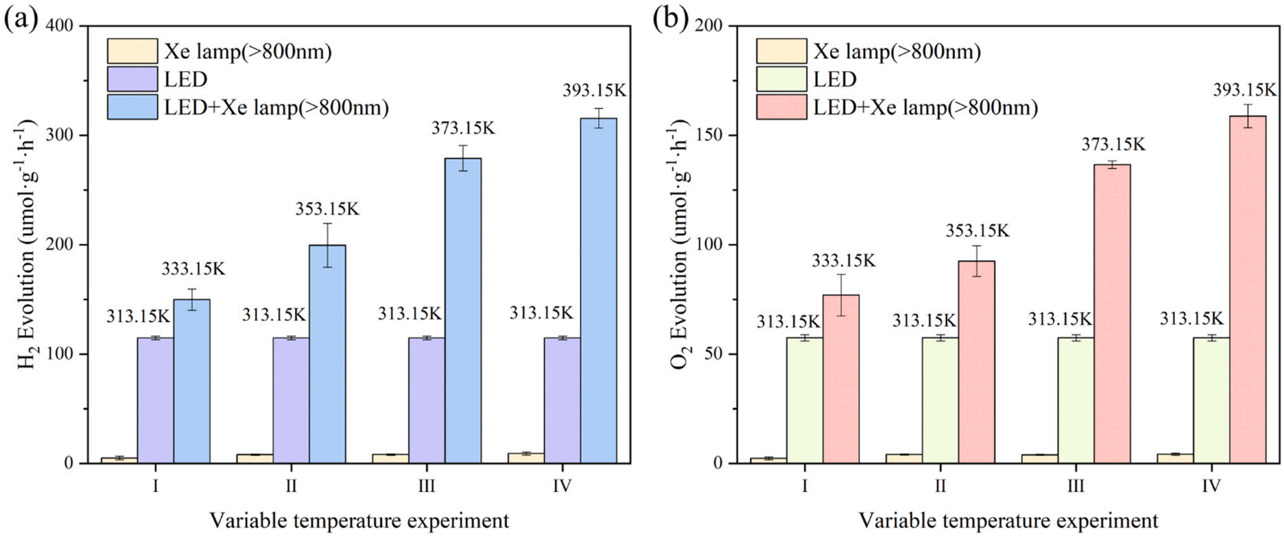

**Fig. 4.** (a) Hydrogen production rates of 0.5 %Ni-MgAlSTO at different temperatures.(b) Oxygen production rates of 0.5 %Ni-MgAlSTO at different temperatures.

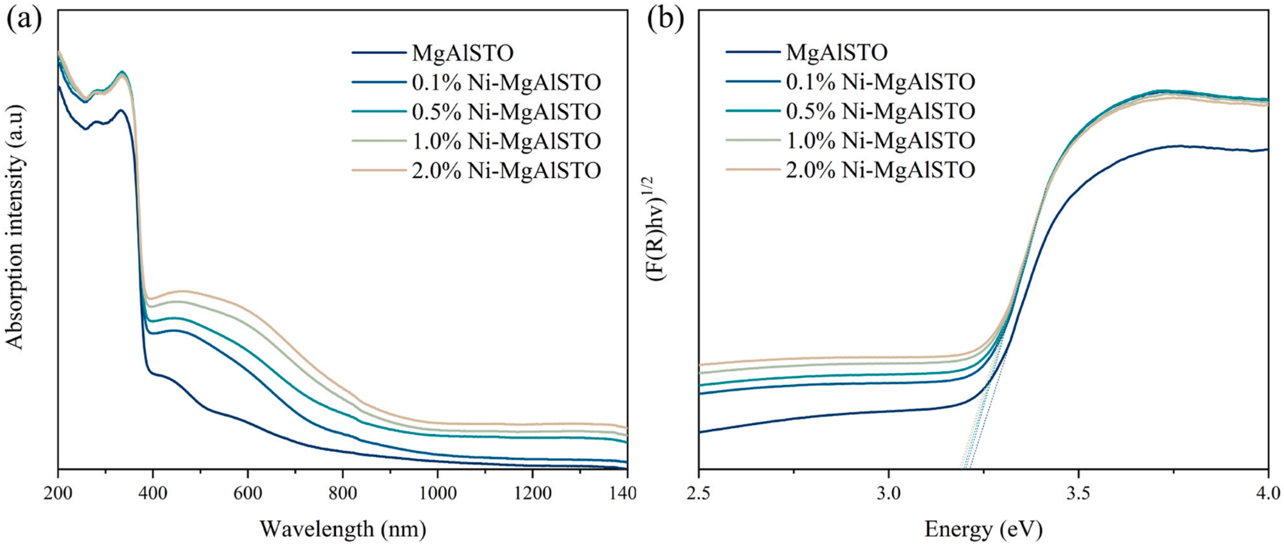

**Fig. 5.** (a) UV–vis absorption spectra and (b) determination of the optical band gap over as-prepared catalysts.

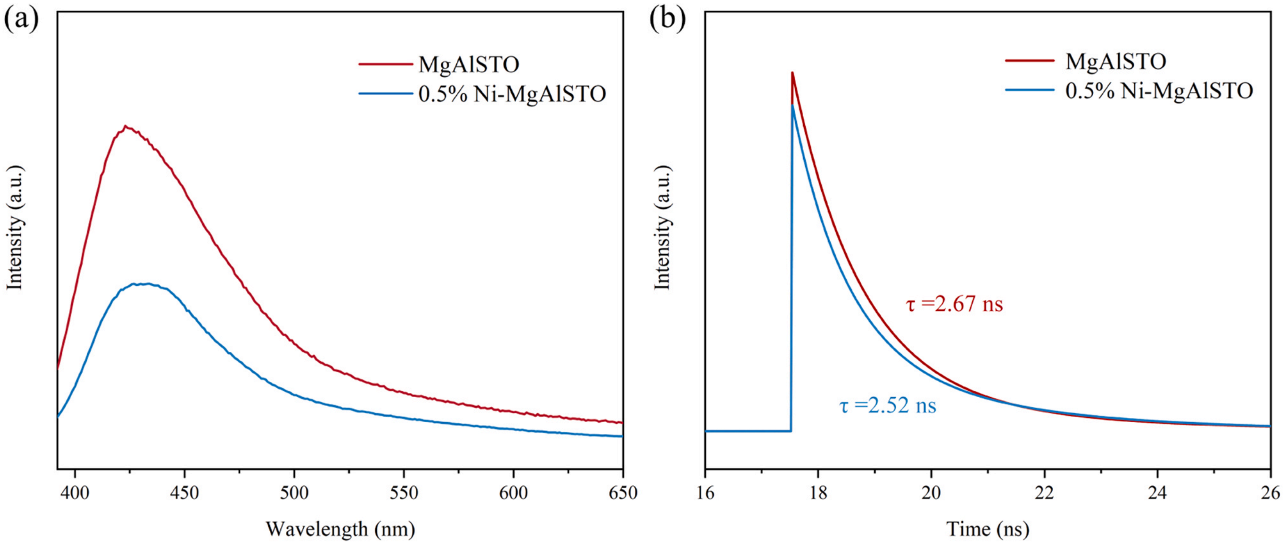

**Fig. 6.** (a) PL spectra and (b) Time-resolved PL emission spectra of catalysts.

photogenerated electrons and holes. Due to the reduction of the photogenerated carrier complexation rate, more photogenerated electrons and holes can participate in the photochemical reaction, thereby enhancing the water decomposition activity. To further evaluate the photogenerated carrier lifetime of the catalytic materials, the results were investigated using time-resolved photoluminescence spectroscopy (TRPL). The TRPL decay curves of the two materials were fitted, as shown in Fig. 6b. The average lifetime of the unloaded MgAlSTO sample was 2.67 ns, while the sample with 0.5 % Ni loading exhibited a slightly shorter lifetime of 2.52 ns. This decrease in carrier lifetime indicates that the heterojunction structure formed between NiOOH and MgAlSTO efficiently extracts and accelerates the transfer of photogenerated electrons and holes, facilitating their rapid separation and enhancing the water splitting process [39].

To further investigate the carrier properties of the materials, transient photocurrent tests were performed. The 0.5 %Ni-MgAlSTO sample exhibited a stronger photocurrent response compared to the pure MgAlSTO samples under the same light conditions. This phenomenon indicated that the introduction of NiOOH significantly improves the separation efficiency of photogenerated carriers in the material. Combined with the UV absorption results, this suggests that the loading of NiOOH improves the UV absorption capability of the material, which effectively enhances the generation of photogenerated carriers, which in turn leads to the enhancement of the photocurrent intensity. To further assess the carrier transport capability, the EIS was employed, the corresponding EIS equivalent circuit fitting is shown in Figure S10 [40]. The size of the arc radius in the impedance spectrum is closely related to the charge transfer resistance of the catalyst [41,42]. By comparing the impedance spectra of different samples, it was observed that the sample loaded with NiOOH has a smaller arc radius in the high-frequency region, signifying a lower charge transfer resistance. This reduction in resistance decreases the recombination probability of carriers, facilitating more efficient charge separation and transport. Additionally, the semiconductor type of the synthesized materials was verified using Mott-Schottky analysis. As shown in Figure S11, both MgAlSTO and 0.5 %Ni-MgAlSTO exhibited positive slopes in their Mott-Schottky plots, confirming that both materials are N-type semiconductors. This indicates that the introduction of NiOOH did not alter the inherent N-type semiconductor characteristics of MgAlSTO.Fig. 7.

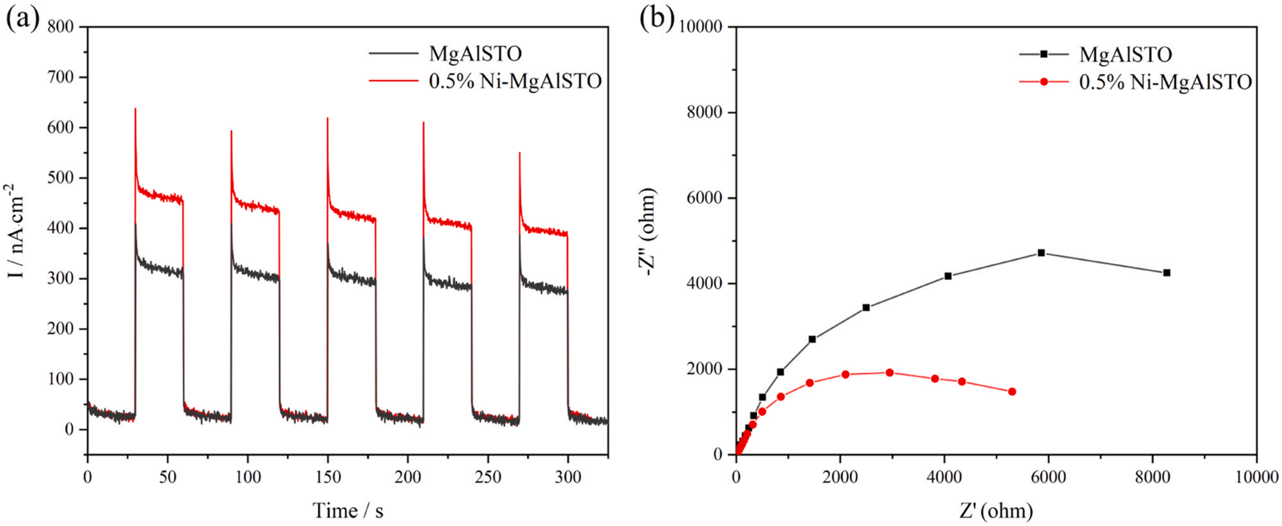

**Fig. 7.** (a) Transient photocurrent and (b) EIS results of catalysts.

### 3.4. *Mechanism of Photothermal Synergistic Reaction*

When sunlight is used as the only energy source, the photothermal synergistic reaction not only increases the surface temperature of the catalyst by the thermal effect but also promotes the reaction via both thermal and non-thermal effects [43]. The temperature change caused by the thermal effect impacts the radiation absorption characteristics of the semiconductor. Therefore, a comprehensive study of how temperature changes induced by photothermal effects influence the radiation absorption properties of semiconductors is essential for optimizing catalytic material design and enhancing solar energy conversion. The radiation absorption spectra of 0.5 %Ni-MgAlSTO material were measured across a temperature range of 313.15 K~393.15 K. As shown in Fig. 8a, the absorption in the UV region was significantly enhanced with increasing temperature, which was consistent with the experimental results. If a xenon lamp filtered at wavelengths below 800 nm were used as an infrared light heat source to increase the reaction temperature in the experiments, the catalytic material would have a significantly enhanced absorption in the UV region (365 nm LED), which would generate more photogenerated carriers to participate in the water decomposition reaction and thus increase the $H_2$ yield. Furthermore, the absorption of visible and infrared light gradually increased with temperature, boosting the material's photothermal conversion performance. In conclusion, the temperature increase due to the thermal effect can significantly enhance the absorption of the catalytic material for the whole spectrum, and the enhanced radiation response of the material was conducive to the photothermal catalytic water decomposition reaction.

From the above analysis, the temperature increase induced by the thermal effect was usually able to effectively enhance the generation of photogenerated carriers, but at the same time, the carrier compounding process also imposes constraints on the effective participation of photogenerated electrons and holes in the reaction. To analyze the radiative recombination behavior of the semiconductor materials at different temperatures, variable-temperature PL measurements were conducted. The intensity of the photoluminescence spectra of 0.5 %Ni-MgAlSTO materials was measured at 313.15 K~393.15 K using a 365 nm laser as the excitation light source. As shown in Fig. 8b, the photoluminescence intensity decreased with increasing temperature, suggesting that higher temperatures weaken the radiative recombination in the material. This reduction in recombination enhances the separation of photogenerated carriers and promotes their involvement in subsequent chemical reactions [44]. The observed decrease in carrier recombination may be related to the semiconductor material's conductivity. As temperature

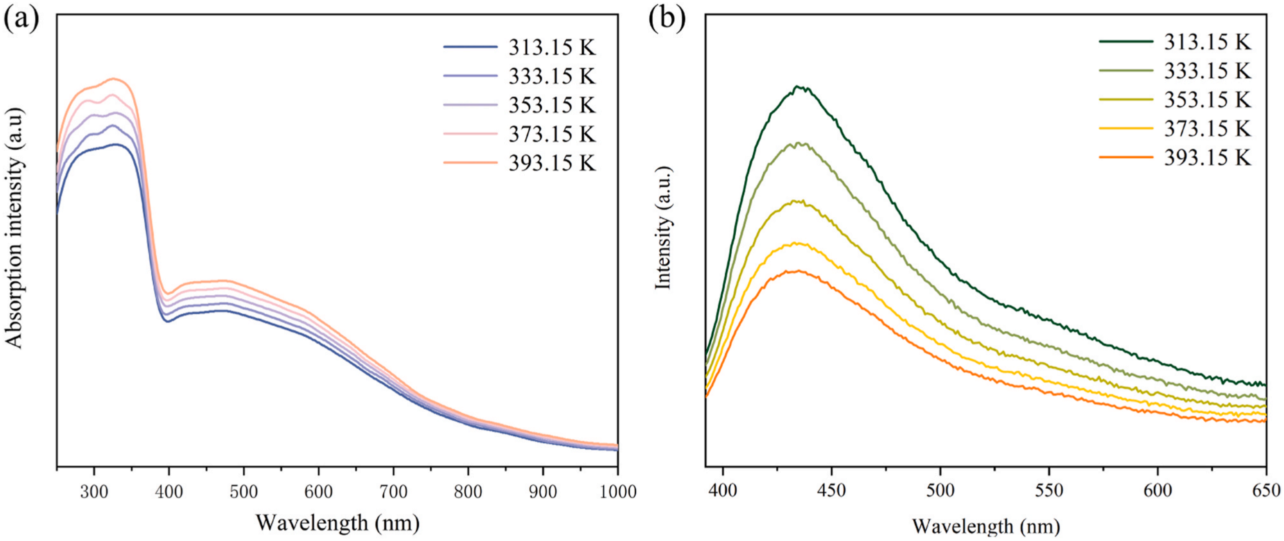

**Fig. 8.** (a) UV−Vis diffuse reflectance spectra and (b) PL spectra of 0.5 %Ni-MgAlSTO at different temperatures.

increases, the conductivity of the semiconductor improves, which reduces the likelihood of carrier recombination within the material. This improvement facilitates the efficient separation and migration of photogenerated carriers, thus increasing the probability of their participation in catalytic reactions. To further evaluate the effect of temperature on carrier lifetime, the 0.5 %Ni-MgAlSTO material was measured at different temperatures using time-resolved photoluminescence spectroscopy (TRPL). As shown in Figure S12, the lifetimes of the catalyst at 313.15 K, 333.15 K, 353.15 K, 373.15 K, and 393.15 K are 2.47 ns, 2.37 ns, 2.26 ns, 2.23 ns, 2.20 ns, and 2.20 ns, respectively. The gradual shortening of the carrier lifetimes with increasing temperature indicates that higher temperatures promote faster transfer and separation of photogenerated carriers. This enhancement in semiconductor conductivity facilitates quicker migration of carriers to the reaction interface, improving the efficiency of the chemical reactions. Therefore, for the radiation response of the 0.5 %Ni-MgAlSTO material, the temperature increase extends the light absorption range of the semiconductor material, especially for the ultraviolet light absorption ability was enhanced. At the same time, the elevated temperature inhibits the radiative recombination of charge carriers, allowing more photogenerated charge carriers to be quickly transferred to the semiconductor surface to participate in the reaction, effectively improving the $H_2$ yield.

To gain insight into the reasons for the changes in catalyst performance at different temperatures, temperature-dependent electrochemical characterization was used to further reveal the mechanism. Due to the temperature limitation of the electrolyte, four temperatures of 293.15 K, 313.15 K, 333.15 K, and 353.15 K were selected as test points, which can reflect the law of the material's radiative properties varying with temperature. The photocurrents of 0.5 %Ni-MgAlSTO material were measured at different temperatures. As shown in Fig. 9a, the photocurrent at the moment of light on will produce obvious spikes and then gradually smooth, this is due to the semiconductor receiving light when the light is turned on will rapidly produce a large number of photogenerated carriers, these carriers in the material will rapidly migrate, with the compound or migration of carriers, the current gradually tends to stabilize. With increasing temperature, the photocurrent response significantly improved. The photocurrent at 353.15 K was nearly twice as high as that at 293.15 K. This indicates that at the same light illumination, the increase in temperature can cause the material to produce more photogenerated carriers, thereby enhancing the photocurrent response.

The EIS of the catalytic materials was tested at different temperatures. As shown in Fig. 9b and Figure S13, the diameter of the arcs in the high-frequency region decreased significantly with temperature, indicating that higher temperatures reduce the migration resistance of photogenerated carriers, which may be one of the reasons for the increase in photocurrent density of the materials with temperature [45,46]. The reason why the migration resistance decreases with increasing temperature is related to the conductivity characteristics of semiconductor materials. The increase in temperature effectively increases the conductivity of the semiconductor, and the conductivity of the semiconductor material depends on the number of free carriers. As the temperature rises, more valence band electrons can overcome the band gap energy and enter the conduction band, thereby generating more free electrons and holes, which can improve the conductivity of the semiconductor material and promote rapid carrier transfer.

Mott-Schottky analysis was performed to assess the changes in carrier concentration at different temperatures. As shown in Figure S14, the slopes of the Mott-Schottky curves for the catalyst at the four temperatures remained positive, confirming that the temperature change did not change the N-type semiconductor properties of the material, and the majority of the carriers in it are still free electrons [47]. According to the Mott-Schottky formula, where a steeper slope corresponds to a lower carrier density. The results show that the average carrier density of the material gradually rises as the temperature is elevated. This change is mainly influenced by two aspects: first, the increase in temperature leads to an increase in the concentration of thermally excited equilibrium carriers in the semiconductor; second, the increase in temperature promotes the absorption of UV light by the semiconductor, resulting in the production of more non-equilibrium carriers. This phenomenon was consistent with test results from UV–visible absorption spectroscopy. Furthermore, the flat-band potentials of the 0.5 %Ni-MgAlSTO material at different temperatures were determined from the Mott-Schottky curves. Its flat-band potentials at 293.15 K, 313.15 K, 333.15 K, and 353.15 K relative to the Ag/AgCl electrode are −0.74 eV, −0.81 eV, −0.92 eV, and −1.0 eV, respectively. A more negative flat band potential usually indicates that its conduction band value was more negative, and thus it can provide photogenerated electrons with a stronger reducing ability, which is beneficial to the hydrogen evolution reaction [48].

Based on the preceding analysis, the excellent water decomposition activity of MgAlSTO material loaded with non-noble metal Ni can be attributed to the synergistic effect of both the photo effect and thermal effect, the mechanism of photothermal synergistic reaction is shown in Fig. 10. In terms of photo effect, $Ni^{2+}$ is selectively deposited on the oxidized crystal surface of MgAlSTO to form NiOOH. The incorporation of NiOOH can significantly enhance the absorption of the full spectrum of the material and reduce the radiation recombination of the material.

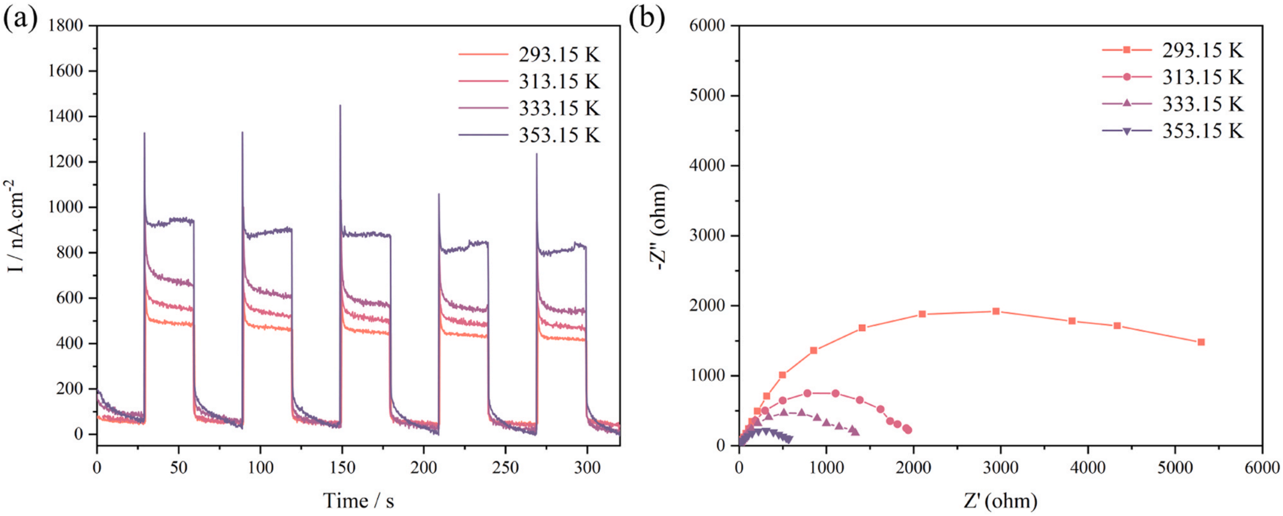

**Fig. 9.** (a) Time-dependent photocurrent result, (b) EIS change of 0.5 %Ni-MgAlSTO at different temperatures.

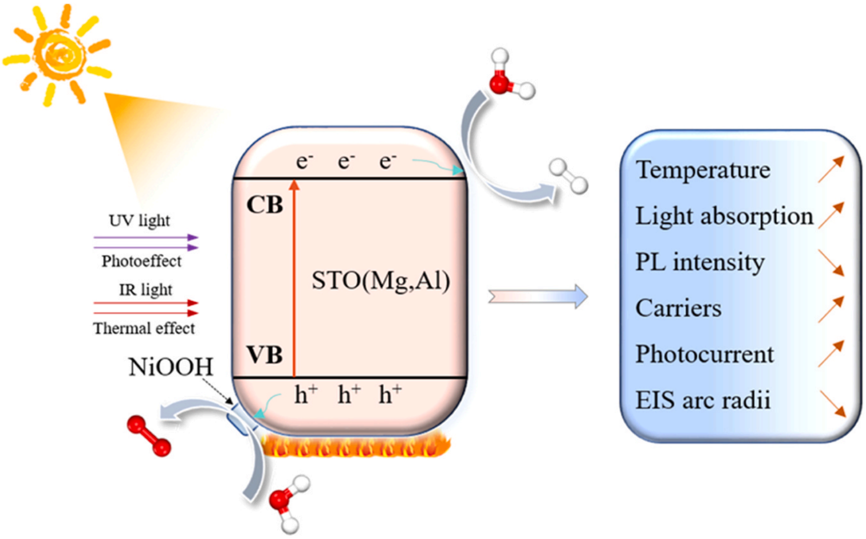

**Fig. 10.** The mechanism of photothermal synergistic water splitting reaction.

However, excessive NiOOH loading will encapsulate the surface of the substrate material, which affects the contact between the water molecules and the material to reduce the $H_2$ yield. The 0.5 %Ni-MgAlSTO has the best water splitting activity. The enhanced absorption of UV light facilitates the generation of more photogenerated carriers in the semiconductor, and the reduced radiation recombination indicates that more photogenerated electrons and holes can participate in the photochemical reaction. Meanwhile, the loading of NiOOH enhances the photocurrent density and lowers the carrier transport impedance. This demonstrates that the cocatalyst promotes the efficient separation and migration of photogenerated carriers, thereby reducing carrier recombination and significantly improving catalytic performance. In terms of thermal effect, the introduction of NiOOH brings about a strong photothermal effect. Temperature measurements reveal that the surface temperature of MgAlSTO material containing NiOOH increases by approximately 40°C compared to pure MgAlSTO, which corresponds to the UV results, due to the loading of NiOOH can enhance the absorption of visible and infrared spectra of the material, which was manifested in the enhancement of photothermal effect. From the experiments in Fig. 3c, the thermal effect plays a crucial role in enhancing the water decomposition reaction. The mechanism of the thermal effect on the water decomposition reaction was further investigated by using spectroscopic experiments and variable temperature characterization. Spectral data indicate that ultraviolet light, with higher energy in the solar spectrum, primarily drives the chemical reaction, while longer-wavelength radiation contributes to the reaction by elevating the temperature through the photothermal effect. For the 0.5 %Ni-MgAlSTO material, the photo-absorption of the catalyst in the full spectrum of sunlight was significantly improved with increasing temperature. The enhanced light absorption in the ultraviolet promotes the generation of more photogenerated carriers, while the increased absorption in the visible and infrared bands enhances the photothermal effect of the catalysts, which contributes to the increase in the surface temperature of the catalysts. The elevated temperature also reduces the radiative recombination of photogenerated carriers, enabling more carriers to participate in the water decomposition reaction. In summary, the temperature increase induced by the thermal effect positively influences both the photo-absorption performance and the carrier behavior of the catalysts, which not only enhances the spectral absorption but also reduces the carrier recombination, and these factors together promote the increase of hydrogen production. Additionally, as the temperature increases, the photocurrent of the semiconductor material increases and the electrical impedance gradually decreases, which allows more photogenerated electrons to migrate to the catalyst surface more efficiently for the reaction. The above analysis explains why the temperature increase caused by the thermal effect can effectively promote the photothermal catalytic water splitting performance. Consequently, the design of catalytic materials with both light and thermal effects can significantly enhance the water splitting activity and promote the effective utilization of solar energy.

## 4. Conclusion

In this study, the non-precious metal Ni loaded MgAlSTO material achieved a photothermal synergistic effect, producing 1011.6 $\mathrm{umol \cdot g^{-1} \cdot h^{-1}}$ of $H_2$ with 497.1 $\mathrm{umol \cdot g^{-1} \cdot h^{-1}}$ of $O_2$, which effectively improves the yield of photothermal catalyzed water decomposition. NiOOH, acting as an oxidation cocatalyst, efficiently extracts holes, promotes the separation of photogenerated electrons and holes, and enhances the migration efficiency of charge carriers, thereby improving the photoresponse of semiconductor materials. Additionally, NiOOH can enhance the absorption of the full spectrum of the material, effectively enhance the photothermal effect, and promote the water decomposition reaction by increasing the surface temperature. Spectroscopic experiments further confirm that under the photothermal synergistic conditions, the $H_2$ yield is enhanced by a factor of 2.7 compared to photocatalytic conditions alone. Detailed variable-temperature characterization reveals that the thermal effect effectively boosts the material's absorption across the full solar spectrum and reduces carrier recombination. Moreover, the increase in temperature leads to a rise in the photocurrent and a decrease in electrical impedance, facilitating the efficient migration of photogenerated electrons to the catalyst surface for the reaction. This collectively enhances the overall efficiency of photothermal catalytic water splitting. Thus, the interplay between optical and thermal effects should be considered when designing photothermal catalytic materials. This work provides a valuable strategy for developing non-noble metal catalysts that leverage photothermal synergy for efficient water splitting.

## CRediT authorship contribution statement

**Mao Jia:** Visualization. **Zhang Entao:** Validation. **Xie Yu:** Formal analysis. **Xu Chenyu:** Writing – review & editing, Project administration. **zhang yanwei:** Project administration, Funding acquisition. **Gao Yuan:** Investigation. **Hong Jianan:** Methodology. **Zhu Xuan:** Writing – original draft, Visualization, Investigation, Formal analysis, Data curation, Conceptualization.

## Declaration of Competing Interest

The authors declare that they have no known competing financial interests or personal relationships that could have appeared to influence the work reported in this paper.

## Acknowledgements

We acknowledge the financial support of the Zhejiang Provincial Natural Science Foundation of China under Grant (LDT23E06014E06), National Natural Science Foundation of China (52341602), Zhejiang Provincial Natural Science Foundation of China under Grant (LQ24E060001), National Key Research and Development Project (2023YFC3710800) and Fundamental Research Funds for the Central Universities (2022ZFJH04).

## Appendix A. Supporting information

Supplementary data associated with this article can be found in the online version at doi:10.1016/j.jallcom.2025.180534.

## Data Availability

All data generated or analyzed during this study are included in this published article and its ESI.†

## References

[1] K. Jayaramulu, S. Mukherjee, D.M. Morales, D.P. Dubal, A.K. Nanjundan, A. Schneemann, J. Masa, S. Kment, W. Schuhmann, M. Otyepka, R. Zbořil, R. A. Fischer, Graphene-based metal–organic framework hybrids for applications in catalysis, environmental, and energy technologies, Chem. Rev. 122 (2022) 17241–17338.

[2] H. Dong, T. Wang, F. Liu, Z. Luo, X. Gao, M. Cai, Unidirectional ice-templating for aerogel adsorbents: excellent pore structure and high $CO_2$ capture performance for direct air capture, Sep. Purif. Technol. 355 (2025) 129588.

[3] W. Raza, K. Ahmad, R.A. Khan, H. Kim, Ag decorated ZnO for enhanced photocatalytic $H_2$ generation and pollutant degradation, Int. J. Hydrog. Energy 48 (2023) 29071–29081.

[4] Z. Wang, Y. Hu, S. Zhang, Y. Sun, Artificial photosynthesis systems for solar energy conversion and storage: platforms and their realities, Chem. Soc. Rev. 51 (2022) 6704–6737.

[5] Z. Kong, D. Zhang, J. Dong, J. Yu, D. Zhang, J. Liu, P. Cai, X. Pu, Cd0.9Zn0.1S/NiB Schottky heterojunction for efficient photothermal-assisted photocatalytic hydrogen evolution, J. Alloy. Compd. 1006 (2024) 176311.

[6] X. Pan, X. Wang, Z. Zhang, C. Ma, J. Chen, Y. Yuan, H. Li, S-scheme γ-Ga2O3/CdS heterojunction with good photocatalytic overall water splitting performance, J. Alloy. Compd. 1013 (2025) 178595.

[7] S. Feng, P. Zhang, Y. Zhang, J. Cao, Y. Zheng, J. Wang, L. Shi, J. Pan, C. Li, Self-cleaning transparent photovoltaic device in perovskite $SrTiO_3$ quantum dot modified $CuGaO_2/Zn_2SnO_4$ nanoarrays pn junction via surface plasma modification, Appl. Phys. Lett. 125 (2024) 091902.

[8] X. Lv, W. Yang, Z. Cai, J. Cao, L. Shi, J. Pan, Z. Zhao, C. Li, Perovskite-based transparent pn junction in CuI/$SrTiO_3$ toward enhanced photoelectric response via interfacial homogeneous perovskite $LaCoO_3$ transition layer, Appl. Phys. Lett. 126 (2025) 091901.

[9] T. Zhang, X. Guan, Z. Zhang, B. Wang, J. Qu, W. Zeng, X. Ye, L. Guo, Photothermal catalytic hydrogen production coupled with thermoelectric waste heat utilization and thermal energy storage for continuous power generation, Nano Energy 121 (2024) 109273.

[10] J. Li, L. Ding, Z. Su, K. Li, F. Fang, R. Sun, Y. Qin, K. Chang, Non-lignin constructing the gas–solid interface for enhancing the photothermal catalytic water vapor splitting, Adv. Mater. 35 (2023) 2305535.

[11] J. Wang, P. Li, C. Liu, J. Liu, G. Li, L. Li, Recent advances in photothermal catalysis: coupling hydrogen evolution and organic conversion, Int. J. Hydrog. Energy 67 (2024) 658–680.

[12] L. Zhang, X. Zhang, H. Mo, J. Hong, S. Yang, Z. Zhan, C. Xu, Y. Zhang, Synergistic modulation between non-thermal and thermal effects in photothermal catalysis based on modified $In_2O_3$, ACS Appl. Mater. Interfaces 15 (2023) 39304–39318.

[13] D. Jin, F. Qiao, Y. Zhou, J. Wang, K. Cao, J. Yang, J. Zhao, L. Zhou, H. Li, Cu/$Mo_2C$ synthesized through Anderson-type polyoxometalates modulate interfacial water structure to achieve hydrogen evolution at high current density, Nano Res. 17 (2024) 2546–2554.

[14] Z. Wang, X. Yuan, H. Guo, X. Zhang, J. Peng, Y. Pan, Rational design principles of single-atom catalysts for hydrogen production and hydrogenation, Energy Environ. Sci. 17 (2024) 8019–8056.

[15] Y. Huang, D. Li, S. Feng, Y. Jia, S. Guo, X. Wu, M. Chen, W. Shi, Pt Atoms/Clusters on Ni-phytate-sensitized carbon nitride for enhanced NIR-light-driven overall water splitting beyond 800nm, Angew. Chem. Int. Ed. 61 (2022) e202212234.

[16] Y. Kim, M. Watanabe, J. Matsuda, J.T. Song, A. Takagaki, A. Staykov, T. Ishihara, Tensile strain for band engineering of $SrTiO_3$ for increasing photocatalytic activity to water splitting, Appl. Catal. B: Environ. 278 (2020) 119292.

[17] Q. Wang, K. Domen, Particulate photocatalysts for light-driven water splitting: mechanisms, challenges, and design strategies, Chem. Rev. 120 (2020) 919–985.

[18] J. Bandara, C. Rajapaksha, C.A. Jayasundera, H. Tan, C.F. Yan, Harnessing of low-energy IR photons via oxygen-vacancies in $SrTiO_3$ nanocrystals for photocatalytic hydrogen production, Int. J. Hydrog. Energy 48 (2023) 17074–17085.

[19] T. Takata, J. Jiang, Y. Sakata, M. Nakabayashi, N. Shibata, V. Nandal, K. Seki, T. Hisatomi, K. Domen, Photocatalytic water splitting with a quantum efficiency of almost unity, Nature 581 (2020) 411–414.

[20] Y.L. Qin, F. Fang, Z.Z. Xie, H.W. Lin, K. Zhang, X. Yu, K. Chang, La,Al-Codoped $SrTiO_3$ as a photocatalyst in overall water splitting: significant surface engineering effects on defect engineering, ACS Catal. 11 (2021) 11429–11439.

[21] X. Zhu, Y. Liu, M. Wang, L. Zhang, Q. Li, E. Zhang, H. Mo, Y. Gao, C. Xu, Y. Zhang, Boosting solar photothermal synergy for efficient overall water splitting based on Mg, Al codoped and Rh/$Cr_2O_3$/CoOOH coloaded $SrTiO_3$, Chem. Eng. J. 479 (2024) 147636.

[22] L.D. de Almeida, H. Wang, K. Junge, X. Cui, M. Beller, Recent advances in catalytic hydrosilylations: developments beyond traditional platinum catalysts, Angew. Chem. Int. Ed. 60 (2021) 550–565.

[23] M. Cai, Z. Wu, Z. Li, L. Wang, W. Sun, A.A. Tountas, C. Li, S. Wang, K. Feng, A.-B. Xu, S. Tang, A. Tavasoli, M. Peng, W. Liu, A.S. Helmy, L. He, G.A. Ozin, X. Zhang, Greenhouse-inspired supra-photothermal $CO_2$ catalysis, Nat. Energy 6 (2021) 807–814.

[24] F. Fang, F. Xu, Z. Su, X. Li, W. Han, Y. Qin, J. Ye, K. Chang, Understanding targeted modulation mechanism in $SrTiO_3$ using $K^+$ for solar water splitting, Appl. Catal. B-Environ. 316 (2022) 121613.

[25] Y. Zhang, X. Wu, Z.-H. Wang, Y. Peng, Y. Liu, S. Yang, C. Sun, X. Xu, X. Zhang, J. Kang, S.-H. Wei, P.F. Liu, S. Dai, H.G. Yang, Crystal facet engineering on $SrTiO_3$ enhances photocatalytic overall water splitting, J. Am. Chem. Soc. 146 (2024) 6618–6627.

[26] H. Lyu, T. Hisatomi, Y. Goto, M. Yoshida, T. Higashi, M. Katayama, T. Takata, T. Minegishi, H. Nishiyama, T. Yamada, Y. Sakata, K. Asakura, K. Domen, An Al-doped $SrTiO_3$ photocatalyst maintaining sunlight-driven overall water splitting activity for over 1000h of constant illumination, Chem. Sci. 10 (2019) 3196–3201.

[27] L.-a Huang, Z. He, J. Guo, S.-e Pei, H. Shao, J. Wang, Photodeposition fabrication of hierarchical layered Co-doped Ni oxyhydroxide ($Ni_xCo_{1-x}OOH$) catalysts with enhanced electrocatalytic performance for oxygen evolution reaction, Nano Res. 13 (2020) 246–254.

[28] Z. Zhang, J. Li, Y.M. Fung, M. Gao, G. Zhong, W. Li, X. Shi, X. Yang, S. Liu, J. Lancok, M. Ma, D.C.C. Lam, UV-assisted expansion of oxyhydroxides surrounding $BiVO_4$ crystals for improved solar water oxidation, Materials 6 (2025) 100279.

[29] F.A. Rabuffetti, H.-S. Kim, J.A. Enterkin, Y. Wang, C.H. Lanier, L.D. Marks, K. R. Poeppelmeier, P.C. Stair, Synthesis-dependent first-order Raman scattering in $SrTiO_3$ nanocubes at room temperature, Chem. Mater. 20 (2008) 5628–5635.

[30] H. Wang, A. Guan, J. Zhang, Y. Mi, S. Li, T. Yuan, C. Jing, L. Zhang, L. Zhang, G. Zheng, Copper-doped nickel oxyhydroxide for efficient electrocatalytic ethanol oxidation, Chin. J. Catal. 43 (2022) 1478–1484.

[31] P.W. Menezes, S. Yao, R. Beltrán-Suito, J.N. Hausmann, P.V. Menezes, M. Driess, Facile access to an active γ-NiOOH electrocatalyst for durable water oxidation derived from an intermetallic nickel germanide precursor, Angew. Chem. Int. Ed. 60 (2021) 4640–4647.

[32] Y. Zhu, P.A. Salvador, G.S. Rohrer, Controlling the relative areas of photocathodic and photoanodic terraces on the $SrTiO_3$ (111) surface, Chem. Mater. 28 (2016) 5155–5162.

[33] P. Wen, R. Lei, X. Cao, Q. Ma, G. Zhang, C. Guo, X. Wang, Y. Qiu, Anchored Ni nanocrystals boosting $BiVO_4$ photoanode for highly efficient water oxidation via in-situ generation of Ni@NiOOH co-catalyst, Chem. Eng. J. 454 (2023) 139983.

[34] Z. Du, Z. Meng, H. Sun, Y. Li, C. Jiang, Y. Li, X. Hu, Y. Cui, S. Yu, H. Tian, Exploring the role of iron in $Fe_5Ni_4S_8$ toward oxygen evolution through modulation of electronic orbital occupancy, J. Energy Chem. 92 (2024) 52–62.

[35] W. Chen, G.-B. Huang, H. Song, J. Zhang, Efficient and stable charge transfer channels for photocatalytic water splitting activity of CdS without sacrificial agents, J. Mater. Chem. A 8 (2020) 20963–20969.

[36] X. Bian, Y. Zhao, G.I.N. Waterhouse, Y. Miao, C. Zhou, L.-Z. Wu, T. Zhang, Quantifying the contribution of hot electrons in photothermal catalysis: a case study of ammonia synthesis over carbon-supported Ru catalyst, Angew. Chem. Int. Ed. 62 (2023) e202304452.

[37] X. Zhang, C. Xu, L. Zhang, Z. Li, J. Hong, Y. Zhang, Photothermal catalytic water splitting at diverse two-phase interfaces based on Cu–$TiO_2$, ACS Appl. Energ. Mater. 5 (2022) 4564–4576.

[38] T. Tangcharoen, J. T-Thienprasert, C. Kongmark, Effect of calcination temperature on structural and optical properties of $MAl_2O_4$ (M = Ni, Cu, Zn) aluminate spinel nanoparticles, J. Adv. Ceram. 8 (2019) 352–366.

[39] R. Li, T. Takata, B. Zhang, C. Feng, Q. Wu, C. Cui, Z. Zhang, K. Domen, Y. Li, Criteria for efficient photocatalytic water splitting revealed by studying carrier dynamics in a model Al-doped $SrTiO_3$ photocatalyst, Angew. Chem. Int. Ed. 62 (2023) e202313537.

[40] S. Zhu, X. Chen, Z. Li, X. Ye, Y. Liu, Y. Chen, L. Yang, M. Chen, D. Zhang, G. Li, H. Li, Cooperation between inside and outside of $TiO_2$: Lattice $Cu^+$ accelerates carrier migration to the surface of metal copper for photocatalytic $CO_2$ reduction, Appl. Catal. B: Environ. 264 (2020) 118515.

[41] H. Li, P. Jing, C. He, Z. Pan, J. Liu, Y. Cui, J. Wang, Interfacial configuration and mechanism insights of an all-solid-state Z-scheme $BaTiO_3/Bi/Bi_2O_3$ heterojunctions for rapid removal of tetracycline antibiotics, Appl. Surf. Sci. 615 (2023) 156416.

[42] P. Jing, C. He, S. Huang, H. Li, J. Liu, Y. Cui, Y. Pu, J. Wang, 2D Z-scheme heterojunction and oxygen deficiency synergistically boosting the photocatalytic activity of a layered $BaTiO_3/BiOIO_3$ composite, Appl. Mater. Today 29 (2022) 101574.

[43] J. Hong, C. Xu, B. Deng, Y. Gao, X. Zhu, X. Zhang, Y. Zhang, Photothermal chemistry based on solar energy: from synergistic effects to practical applications, Adv. Sci. 9 (2022) 2103926.

[44] X. Li, J. Lin, J. Li, H. Zhang, X. Duan, H. Sun, Y. Huang, Y. Fang, S. Wang, Temperature-induced variations in photocatalyst properties and photocatalytic hydrogen evolution: differences in UV, visible, and infrared radiation, ACS Sustain. Chem. Eng. 9 (2021) 7277–7285.

[45] X.J. Li, H.Y. Zhang, Y.Z. Liu, X.G. Duan, X.Y. Xu, S.M. Liu, H.Q. Sun, S.B. Wang, Synergy of NiO quantum dots and temperature on enhanced photocatalytic and thermophoto hydrogen evolution, Chem. Eng. J. 390 (2020) 124634.

[46] K. Guo, J. Ding, Z. Han, J. Liu, X. Yang, P. Hu, Y. Jiao, F. Teng, Construction a quasi-solid-state photoelectrochemical type photodetector based on $WO_3$/PVA/$ZnSO_4$ and its application in near ultraviolet light detection, Surf. Interfaces 49 (2024) 104422.

[47] Y.C. Du, Y.R. Xue, C. Zhang, Y.X. Liu, Y. Fang, C.Y. Xing, F. He, Y.L. Li, Photoinduced electrocatalysis on 3D flexible OsOx quantum dots, Adv. Energy Mater. 11 (2021) 2100234.

[48] X. Liang, X. Wang, X. Zhang, S. Lin, M. Ji, Q. Liu, M. Wang, Generation of lattice strain in CdS promotes photocatalytic reduction of $CO_2$, ACS Catal. 14 (2024) 4648–4655.